Co-prime Sampling based Time-Delay Estimation for Roadway Survey by Ground Penetrating Radar via Off-Grid Sparse Bayesian Learning

Jingjing Pan, Huimin Pan, Meng Sun, Yide Wang, Vincent Baltazart, Xudong Dong, Jun Zhao, Xiaofei Zhang, Hing Cheung So

Co-prime Sampling based Time-Delay Estimation for Roadway Survey by Ground Penetrating Radar via Off-Grid Sparse Bayesian Learning

Jingjing Pan, Huimin Pan, Meng Sun, *Senior Member, IEEE,* Yide Wang, *Senior Member, IEEE,* Vincent Baltazart, Xudong Dong, Jun Zhao, Xiaofei Zhang and Hing Cheung So, *Fellow, IEEE,*

***Abstract*—Time-delay estimation (TDE) using ground penetrating radar (GPR) is of great importance in roadway surveys. The conventional GPR methods apply uniform sampling strategy for TDE, which require numerous frequency sampling points, leading to lengthy data acquisition time and large data storage, especially for ultra-wideband (UWB) radar. Moreover, detecting the overlapped backscattered echoes from thin layer of roadways remains a challenge in TDE, due to the limited resolution of GPR and the characteristics of GPR signals. To address these issues, we derive a co-prime sampling strategy based TDE for thin layers in roadway survey by exploiting off-grid sparse Bayesian learning (OGSBL), referred as co-prime-OGSBL. In our scheme, the sampling rate of GPR signals with co-prime sampling strategy is greatly reduced compared with the uniform sampling, which therefore reduces the data acquisition burden and computational complexity. The estimation performance of time-delays and thickness is also enhanced with OGSBL by utilizing radar pulse, co-prime sampling, and non-circularity of GPR signals. Both simulation and experimental results demonstrate the efficiency and accuracy of the proposed method in the estimation of time-delays and thickness.**

***Index Terms*—Co-prime sampling, time-delay estimation (TDE), off-grid sparse Bayesian learning (OGSBL), ground penetrating radar (GPR).**

I. Introduction

ROADWAY is one of the major infrastructures in modern transportation systems. However, due to anthropopic or environmental factors, such as traffic loads and rainfall, roadway often suffers distress, leading to structural and functional deterioration like cracks, internal voids, and debonding [1]–[4]. Therefore, roadway maintenance becomes more and more critical for the safety of transportation, and the rapid and accurate survey of roadways is gaining significance [5], [6]. The early damages of the roadway can be detected by monitoring the responses from road pavement structure through various non-destructive testing (NDT) methods [7]–[10]. Among them, ground penetrating radar (GPR) is one of the most effective tools, which has many applications in civil engineering, such as bridge and building evaluation, mapping of pipelines as well as roadway survey [10]–[15].

In civil engineering, roadways are usually modeled as horizontally stratified media [16], [17]. As a result, radar profiles can be used to determine the vertical structure of roadways through echo detection and amplitude estimation. Specifically, echo detection provides time-delay estimation (TDE) for each interface, while amplitude estimation can retrieve the wave speed within each layer [16], [18].

In recent years, thin pavement surfacing has gained much popularity as a cost-effective and sustainable solution for maintaining and rehabilitating roadways [16], [17], [19]. However, the back-scattered echoes of thin thickness roadways would be too close to be distinguished by classical GPR data systems. High-resolution signal processing methods, such as MUSIC and ESPRIT, are therefore needed to improve the temporal resolution of GPR system [16], [20]–[23]. Another challenge in the interpretation of GPR signals is the strong correlation between echoes, due to multipath propagation. Decorrelation techniques, like spatial smoothing preprocessing and its variants [24], are required in some GPR procedures, especially with high resolution subspace methods.

In the literature, within a given frequency bandwidth, the uniform sampling strategy is usually applied on the impulse GPR signals in the frequency domain or by a step-frequency GPR [25]–[27]. However, GPR measurements with uniform sampling frequencies are often burdened by large data volumes, especially for ultra-wideband (UWB) GPR and real-time operations. As opposed to uniform sampling using dense, equispaced sampling points, non-uniform sampling achieves unambiguous, accurate estimation with sparse, non-equispaced and less sampling points, which has attracted great interest of researchers. Among the non-uniform sampling, nested sampling and co-prime sampling [28], [29] are two representative strategies because they are implementation friendly and have been widely used in direction of arrival (DOA) estimation, and frequency estimation [29]–[31]. In principle, both the time-delay and DOA can be represented as phase shift in the received data, through which we can construct the "array manifold" of the corresponding parameters. Therefore, in this paper, we adopt the design of co-prime sampling strategy in GPR, which could improve the quality of GPR signals and ensure accurate and timely interpretation.

In nested sampling [31], part of the sampling points are still under Nyquist sampling, and its implementation in GPR signals might suffer from information loss in the high-frequency band. Co-prime sampling is conceptually simple with two interleaved uniform sampling sequences and has a closed-form expression [28], [29]. However, the sparsity in co-prime sampling often leads to ambiguity problems. Numerous signal processing methods have been proposed to deal with sparsity and ambiguity, which can be classified into two typical ap-

proaches. The first mainly makes use of the co-prime property of two physical sub-sequences [28]. The second operates from the perspective of virtual array sequence, that is, the difference/sum co-arrays constructed from cross correlation statistics [29].

However, the virtual sequence based co-prime sampling approaches are under the assumption of uncorrelated signals, which is not applicable for coherent GPR signals. There are works reconstructing the Topelitz matrix through physical array interpolation for decorrelation [32], [33]. In [32], the missing information in the physical sequence is recovered by nuclear norm minimization despite of coherency among signals. To deal with the phase difference problems in [32], [33] proposes to reconstruct a Hermitian Toeplitz matrix through atomic norm minimization with multiple measurement vectors. But these methods these methods are based on the cross-correlation information for matrix reconstruction which might affect the accuracy.

Compressive sensing-based methods, like second-order cone programming (SOCP) and orthogonal matching pursuit (OMP) [17], [34], [35], can work on signal model instead of data covariance matrix and therefore handle coherent signals directly. In [17], a modified OMP method is proposed for TDE in the presence of rough interferences. Later, the performance of [35] is enhanced by using singular value decomposition (SVD) for weak signals coming from pavement layers with similar permittivity. Nevertheless, these methods are highly dependent on the over-complete dictionary. If the true time-delays of the back-scattered echoes do not fall within the grid points of over-complete dictionary, the performance of compressive sensing based methods may drop drastically. Based on the off-grid model, joint orthogonal matching pursuit (JOMP) [36] employs the first order Taylor compensation to improve the DOA estimation in each iteration. However, even if the off-grid data model is adopted for OMP [36]–[38], their performance still declines dramatically for overlapping echoes due to Rayleigh limitation.

Motivated by the aforementioned issues in GPR data processing for roadway surveys, we propose a co-prime frequency sampling strategy combined with off-grid sparse Bayesian learning (OGSBL), called co-prime-OGSBL, for the estimation of time-delays and thickness. In [39], authors exploit the sparsity information of signals from a Bayesian perspective, which has a higher resolution compared to OMP [40]–[42]. The off-grid approach contributes to reducing the impact of over-complete dictionary in parameter estimation. Besides, the characteristic of radar pulse and non-circularity of GPR signals are considered in the proposed method for accurate interpretation of GPR signals. The main contributions of this paper are summarized as:

1) Unlike conventional uniform sampling, co-prime sampling is exploited to reduce the GPR frequency sampling rate in road surveys.
2) In the framework of sparse sampling, OGSBL is adapted for coherent GPR signals, by taking the radar pulse and non-circularity of GPR signals into account.

The remainder of the paper is organized as follows. The radar data model taking into account the co-prime sampling strategy and non-circularity of GPR signals is presented in Section II. In Section III, the proposed TDE method based on OGSBL is described. Sections IV and V provide the simulation and experimental results of the co-prime-OGSBL, respectively. Conclusions are drawn in Section VI.

II. Radar data model

The top layers of an asphalt pavement are studied. Based on the work in [43], [44], the media can be considered as low-loss media, whose dispersivity is negligible. Accordingly, in the far-field condition, the backscattered echoes in frequency domain can be written as [26]

$$y(f) = \sum_{k=1}^{K} \tilde{e}(f) s_k e^{-j2\pi f \tau_k} + n(f), \tag{1}$$

where

- K denotes the number of backscattered echoes, assumed to be known;
- $\tilde{e}(f)$ is the radar pulse in frequency domain, which can be measured as the echo backscattered from a metallic plane;
- s_k represents the amplitude of the kth backscattered echo (depends on the reflection coefficient of the media), which is real in the scenario of low-loss media [44];
- τ_k denotes the arrival time of the kth echo;
- $n(f)$ is an additive white Gaussian noise with zero mean and variance σ^2.

In this paper, the TDE problem is based on the following assumptions:

1) the number of backscattered ehoes, K, is *a priori* known, which is equal to the number of layers in the TDE problem.
2) permittivities of layers can be obtained by amplitude estimation methods, which is not focus in TDE problem of GPR signal.

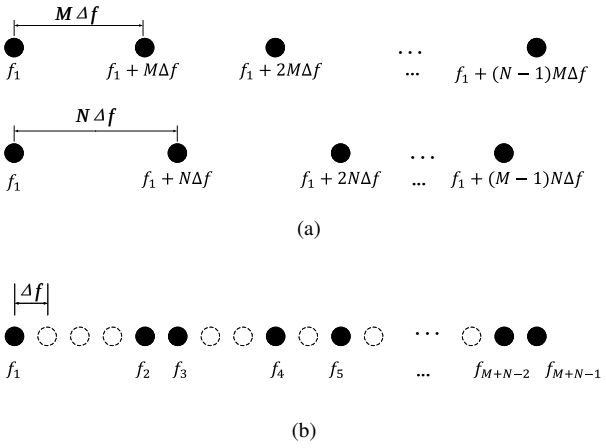

Fig. 1. Frequency sampling in GPR: (a) Two sets of sparse uniform sampling; (b) Co-prime sampling.

A. Co-prime Sampling Model

Inspired by the co-prime technique, we apply the co-prime sampling strategy in the survey of asphalt pavement with GPR. The equispaced frequency sampling points with frequency interval Δf are replaced by a series of nonuniform frequency sampling points accordingly. The co-prime sampling scheme is composed of two subsets of sparsely equispaced sampling points as shown in Fig. 1(a), where M and N ($N < M$) are co-prime integers. Let the frequency interval of the M frequency sampling points be $N\Delta f$ and that with N frequency sampling points be $M\Delta f$. Based on the co-prime property, the sampling points of the co-prime pair do not overlap except the aligned one, which is the reference frequency point.

The co-prime sampling strategy generates non-equispaced sampling points as shown in Fig. 1(b), which makes GPR data processing difficult under the framework of traditional methods. Nevertheless, the frequency points of each subset are fixed. To begin with, we define the mode vectors corresponding to each subset:

$$\begin{aligned}\mathbf{a}_M(\tau_k) = [&e^{-j2\pi f_1\tau_k}, e^{-j2\pi(f_1+N\Delta f)\tau_k},\\ &\ldots, e^{-j2\pi(f_1+(M-1)N\Delta f)\tau_k}]^T\end{aligned} \tag{2}$$

and

$$\begin{aligned}\mathbf{a}_N(\tau_k) = [&e^{-j2\pi f_1\tau_k}, e^{-j2\pi(f_1+M\Delta f)\tau_k},\\ &\ldots, e^{-j2\pi(f_1+(N-1)M\Delta f)\tau_k}]^T.\end{aligned} \tag{3}$$

It is notable that the backscattered echoes of each subset are sampled independently which can be written in the following vector forms as:

$$\mathbf{y}_M = \mathbf{\Lambda}_M\mathbf{A}_M\mathbf{s} + \mathbf{n}_M, \tag{4}$$

$$\mathbf{y}_N = \mathbf{\Lambda}_N\mathbf{A}_N\mathbf{s} + \mathbf{n}_N, \tag{5}$$

where

- $\mathbf{A}_M = [\mathbf{a}_M(\tau_1), \ldots, \mathbf{a}_M(\tau_K)]$ and $\mathbf{A}_N = [\mathbf{a}_N(\tau_1), \ldots, \mathbf{a}_N(\tau_K)]$ are the mode matrices corresponding to the subsets with M and N frequency points, respectively;
- $\mathbf{\Lambda}_M = \text{diag}\{\tilde{e}(f_1), \tilde{e}(f_1 + N\Delta f), \ldots, \tilde{e}(f_1 + (M-1)N\Delta f)\}$ and $\mathbf{\Lambda}_N = \text{diag}\{\tilde{e}(f_1), \tilde{e}(f_1 + M\Delta f), \ldots, \tilde{e}(f_1 + (N-1)M\Delta f)\}$ denote the radar pulses in frequency domain corresponding to the subsets with M and N frequency points, respectively;
- $\mathbf{n}_M \in \mathbb{C}^{M\times 1}$ and $\mathbf{n}_N = \in \mathbb{C}^{N\times 1}$ denote the noise vectors corresponding to the subset with M and N frequency points, respectively.

Then the received signal from co-prime sampling is obtained by stacking sparse sampling vectors $\mathbf{y}_M$ and $\mathbf{y}_N$ as follows

$$\mathbf{y}_C = \begin{bmatrix}\mathbf{y}_M\\ \mathbf{y}_N\end{bmatrix} = \mathbf{\Lambda}_C\mathbf{A}_C\mathbf{s} + \mathbf{n}_C \tag{6}$$

where the mode matrix and mode vectors become $\mathbf{A}_C = [\mathbf{a}_C(\tau_1), \mathbf{a}_C(\tau_2), \cdots, \mathbf{a}_C(\tau_K)]^T$ and $\mathbf{a}_C(\tau_k) = [\mathbf{a}_M^T(\tau_k), \mathbf{a}_N^T(\tau_k)]^T$, respectively. Correspondingly, the radar pulse becomes $\mathbf{\Lambda}_C = \text{diagblk}\{\mathbf{\Lambda}_M, \mathbf{\Lambda}_N\}$, where diagblk$\{\bullet\}$ returns a block-diagonal matrix. And $\mathbf{n}_C = [\mathbf{n}_M^T, \mathbf{n}_N^T]^T$ is the additive Gaussian noise vector of coprime sampling. Apparently, co-prime sampling reduces the frequency sampling points compared with that of the conventional uniform sampling strategy.

B. Extended Radar Data

As the pavement is assumed to be a low-loss media, the backscattered echoes are real and can be regarded as non-circular signals (s_k, $k = 1, 2, ..., K$, is real). Exploiting the characteristic of non-circular signals, the radar data model can be extended by the co-prime sampling model (6) and its conjugate components [45]:

$$\begin{aligned}\mathbf{y} &= \begin{pmatrix}\mathbf{J}\mathbf{y}_C^*\\ \mathbf{y}_C\end{pmatrix}\\ &= \begin{pmatrix}\mathbf{J}\mathbf{\Lambda}_C^*\mathbf{A}_C^* & 0\\ 0 & \mathbf{\Lambda}_C\mathbf{A}_C\end{pmatrix}\begin{pmatrix}\mathbf{s}^*\\ \mathbf{s}\end{pmatrix} + \begin{pmatrix}\mathbf{J}\mathbf{n}_C^*\\ \mathbf{n}_C\end{pmatrix}\\ &= \begin{pmatrix}\mathbf{J}\mathbf{\Lambda}_C^* & 0\\ 0 & \mathbf{\Lambda}_C\end{pmatrix}\begin{pmatrix}\mathbf{A}_C^*\\ \mathbf{A}_C\end{pmatrix}\mathbf{s} + \begin{pmatrix}\mathbf{J}\mathbf{n}_C^*\\ \mathbf{n}_C\end{pmatrix}\\ &= \mathbf{\Lambda}\mathbf{A}\mathbf{s} + \mathbf{n}_E\end{aligned} \tag{7}$$

with $(2M + 2N - 2) \times K$ mode matrix $\mathbf{A}$, $(2M + 2N - 2) \times (2M + 2N - 2)$ diagonal matrix $\mathbf{\Lambda}$, $(2M + 2N - 2) \times 1$ noise vector $\mathbf{n}_E$ and $(M + N - 1) \times (M + N - 1)$ anti-identity matrix (exchange matrix) $\mathbf{J}$. The operator $*$ denotes the complex conjugate. According to the extended radar data model, the new mode vector $\mathbf{a}$ with $(2M + 2N - 2) \times 1$ dimension can be expressed as

$$\begin{aligned}\mathbf{a}(\tau) &= \begin{pmatrix}\mathbf{a}_C^*(\tau)\\ \mathbf{a}_C(\tau)\end{pmatrix}\\ &= [\, e^{2j\pi f_1\tau}, \, e^{2j\pi f_2\tau}, \ldots, e^{2j\pi f_{M+N-1}\tau},\\ &\quad e^{-2j\pi f_1\tau}, e^{-2j\pi f_2\tau}, \ldots, e^{-2j\pi f_{M+N-1}\tau}]^T.\end{aligned} \tag{8}$$

By using the characteristic of non-circular GPR signals, the used frequency band has been increased twice ($2(N-1)M\Delta f$ compared with $(N-1)M\Delta f$) [45]. GPR time resolution can be significantly improved by applying the extended radar data model [46], [47]. In the following, the extended radar data model is used for TDE.

III. Adaptive off-grid sparse Bayesian learning for time-delay estimation

In this section, off-grid sparse Bayesian learning (OGSBL) is employed for TDE of backscattered echoes.

A. Off-Grid Radar Data Model

Firstly, we construct an overcomplete dictionary matrix of the entire GPR working period, which can be sampled as $\mathbf{T} = [t_1\ t_2 \ldots t_{N_s}]$, with $N_s \gg K$ and $\Delta t = t_{i+1} - t_i$. Assuming that the time-delay of the kth backscattered echo $\tau_k \notin \mathbf{T}$, and t_{ik} is the nearest sample point to τ_k, $ik = 1, 2, \ldots . N_s$, the mode vector can be approximated as [39]

$$\begin{aligned}\mathbf{a}(\tau_k) &\approx \mathbf{a}(t_{ik}) + \mathbf{b}(t_{ik})(\tau_k - t_{ik})\\ &= \mathbf{a}(t_{ik}) + \mathbf{b}(t_{ik})\psi_i\end{aligned} \tag{9}$$

where $\mathbf{b}(t_{ik}) = \dfrac{d\mathbf{a}(t_{ik})}{dt_{ik}}$ and $\psi_i \in \{-\frac{\Delta t}{2}, \frac{\Delta t}{2}\}$, $i = 1, 2, \ldots, N_s$.

Define matrices $\mathbf{A}_s$ and $\mathbf{B}_s$ as

$$\mathbf{A}_s = [\mathbf{a}(t_1), \mathbf{a}(t_2), \ldots, \mathbf{a}(t_{N_s})]$$

and

$$\mathbf{B}_s = [\mathbf{b}(t_1), \mathbf{b}(t_2), \ldots, \mathbf{b}(t_{N_s})].$$

Then, we construct an overcomplete dictionary of off-grid radar data model as

$$\mathbf{\Xi} = \mathbf{A}_s + \mathbf{B}_s \mathbf{\Psi} \tag{10}$$

where $\mathbf{\Psi} = \text{diag}\{\boldsymbol{\psi}\}$ and $\boldsymbol{\psi} = [\psi_1, \psi_2, \ldots, \psi_{N_s}]^T$ follows a uniform prior distribution with $p(\boldsymbol{\psi}) = U\left(\left\{-\dfrac{\Delta t}{2}, \dfrac{\Delta t}{2}\right\}^{N_s}\right)$, which is the off-grid parameter and represents the deviation between the true time-delay and the discrete sample point in time domain.

By incorporating the approximate error into noise, the sparse off-grid radar data model can be written as

$$\mathbf{y} = \mathbf{\Lambda \Xi x} + \mathbf{n} \tag{11}$$

where $\mathbf{x} = [x_1, x_2, \ldots, x_{N_s}]$ and $\mathbf{n}$ is the corresponding noise vector. According to [39], noise in (11) follows the Gaussian distribution with zero mean and covariance $\hat{\sigma}^2 \mathbf{I}_{N_s}$. The elements in $\mathbf{x}$ are defined as

$$x_i = \begin{cases} s_k & t_i = t_{ik} \text{ or } t_i = \tau_k \\ 0 & \text{otherwise.} \end{cases} \tag{12}$$

It can be concluded that the off-grid radar data model applies the first-order approximation of (7), which has much smaller estimation error than that of the conventional on-grid model [48].

B. Adaptive Bayesian Learning Method

The likelihood function of GPR backscattered echoes for a single snapshot can be expressed as

$$\begin{aligned} & p\left(\mathbf{y} \left| \mathbf{x}; \hat{\sigma}^2 \mathbf{I}_{N_s} \right.\right) \\ =& \frac{1}{\left(\pi |\hat{\sigma}^2 \mathbf{I}_{N_s}|\right)^{\frac{N_s}{2}}} \exp\left\{\frac{-(\mathbf{y} - \mathbf{\Lambda \Xi x})^H \left(\hat{\sigma}^2 \mathbf{I}_{N_s}\right)^{-1} (\mathbf{y} - \mathbf{\Lambda \Xi x})}{2}\right\} \\ =& \frac{1}{\left(\pi \hat{\sigma}^2\right)^{N_s/2}} \exp\left\{-\frac{\|\mathbf{y} - \mathbf{\Lambda \Xi x}\|_2^2}{2\hat{\sigma}^2}\right\}. \end{aligned} \tag{13}$$

The snapshots of the backscattered echoes are independent from each other. For N_t snapshots, (11) becomes:

$$\mathbf{Y} = \mathbf{\Lambda \Xi X} + \mathbf{N} \tag{14}$$

where $\mathbf{X} = [\mathbf{x}_1, \mathbf{x}_2, \ldots, \mathbf{x}_{N_t}]$, $\mathbf{N} = [\mathbf{n}_1, \mathbf{n}_2, \ldots, \mathbf{n}_{N_t}]$ and its likelihood function is:

$$p(\mathbf{Y}|\mathbf{X}; \boldsymbol{\psi}, \hat{\sigma}^2) = \prod_{j=1}^{N_t} p(\mathbf{y}_j | \mathbf{x}_j; \boldsymbol{\psi}, \hat{\sigma}^2). \tag{15}$$

In Bayesian learning, each column of $\mathbf{X}$ is assumed to follow Gaussian distribution with zero mean, unknown covariance $\mathbf{\Gamma} = \text{diag}\{\boldsymbol{\gamma}_x\}$, and $\boldsymbol{\gamma}_x = [\gamma_1, \gamma_2, \ldots, \gamma_{N_s}]$. The prior distribution of $\mathbf{X}$ is:

$$p\left(\mathbf{X} \left| \boldsymbol{\gamma}_x \right.\right) = \prod_{j=1}^{N_t} \mathcal{CN}\left(\mathbf{x}_j \left| \mathbf{0}_{N_s \times 1}, \mathbf{\Gamma} \right.\right) \tag{16}$$

where $\boldsymbol{\gamma}_x$ determines the sparsity of the model, and the estimated time-delays are obtained by searching the non-zero values of $\boldsymbol{\gamma}_x$ in time domain $\mathbf{T}$. We assume that a Gamma prior is applied on $\boldsymbol{\gamma}_x$ and

$$p(\boldsymbol{\gamma}_x) = \prod_{k=1}^{N_s} \Gamma(\gamma_k | 1, \rho) \tag{17}$$

where ρ is a positive constant value [49].

In TDE of low-loss media, the amplitude of the kth backscattered echo s_k is dependent on the reflection coefficient of the media, which does not change with snapshots ($\mathbf{x}_1 = \cdots = \mathbf{x}_{N_t} = \mathbf{x}$). Therefore, (16) is reduced to

$$p\left(\mathbf{X} \left| \boldsymbol{\gamma}_x \right.\right) = \mathcal{CN}\left(\mathbf{x} \left| \mathbf{0}_{N_s \times 1}, \mathbf{\Gamma} \right.\right).$$

In addition, the inverse of the noise variance $\gamma_0 = \frac{1}{\hat{\sigma}^2}$ is assumed to follow the Gamma prior distribution with $p(\gamma_0) = \Gamma(\gamma_0 | c, d)$, where c and d are set to be close to 0 [49]. Then, we calculate the posterior distribution of $\mathbf{X}$ as

$$p(\mathbf{X}|\mathbf{Y}; \boldsymbol{\psi}, \gamma_0, \boldsymbol{\gamma}_x) = \frac{p(\mathbf{Y}|\mathbf{X}; \boldsymbol{\psi}, \gamma_0) p(\mathbf{X}|\boldsymbol{\gamma}_x)}{p(\mathbf{Y}; \boldsymbol{\psi}, \gamma_0, \boldsymbol{\gamma}_x)}. \tag{18}$$

Afterwards, the joint probability density function (PDF) of the Bayesian model is obtained as

$$p(\mathbf{X}, \mathbf{Y}, \gamma_0, \boldsymbol{\gamma}_x, \boldsymbol{\psi}) = p(\mathbf{Y}|\mathbf{X}, \gamma_0, \boldsymbol{\psi}) p(\mathbf{X}|\boldsymbol{\gamma}_x) p(\boldsymbol{\gamma}_x) p(\gamma_0) p(\boldsymbol{\psi}). \tag{19}$$

According to the principle of Bayesian learning [49], [50], the posterior distribution of $\mathbf{X}$ also follows Gaussian distribution with

$$p\left(\mathbf{X} \left| \mathbf{Y}; \boldsymbol{\psi}, \boldsymbol{\gamma}_x, \gamma_0 \right.\right) = \prod_{j=1}^{N_t} \mathcal{CN}\left(\mathbf{x}_j \left| \boldsymbol{\mu}_j, \mathbf{\Sigma} \right.\right)$$

where

$$\mathbf{\Sigma} = \left(\gamma_0 (\mathbf{\Lambda \Xi})^H \mathbf{\Lambda \Xi} + \mathbf{\Gamma}^{-1}\right)^{-1}.$$

Let $\mathbf{U} = [\boldsymbol{\mu}_1, \boldsymbol{\mu}_2, \ldots, \boldsymbol{\mu}_{N_t}]$, we have:

$$\begin{aligned} \mathbf{U} &= \gamma_0 \mathbf{\Sigma} (\mathbf{\Lambda \Xi})^H [\boldsymbol{y}_1, \boldsymbol{y}_2, \ldots, \boldsymbol{y}_{N_t}] \\ &= \gamma_0 \mathbf{\Sigma} (\mathbf{\Lambda \Xi})^H \mathbf{Y}. \end{aligned}$$

Similar to [51], the parameters γ_k ($k = 1, \cdots, N_s$), γ_0 and $\boldsymbol{\psi}$ can be updated as

$$\gamma_k^{new} = \frac{-N_t + \sqrt{N_t^2 + 4\rho [\mathbf{U}\mathbf{U}^H + \mathbf{\Sigma}]_{k,k}}}{2\rho}, \tag{20}$$

$$\gamma_0^{\text{new}} = \frac{(2M + 2N - 2)N_t + c - 1}{d + ||\mathbf{Y} - \mathbf{\Lambda \Xi U}_j||_2^2 + N_t tr\left(\mathbf{\Lambda \Xi \Sigma \Lambda \Xi}^H \mathbf{\Lambda}^H\right)}, \tag{21}$$

and

$$\begin{aligned}\boldsymbol{\psi}^{\text{new}} &= \arg \min_{\boldsymbol{\psi}\in\{-\frac{\Delta t}{2},\frac{\Delta t}{2}\}} E\left\{||\mathbf{Y}-\boldsymbol{\Lambda}\boldsymbol{\Xi}\mathbf{X}||_2^2\right\} \\ &= \arg \min_{\boldsymbol{\psi}\in\{-\frac{\Delta t}{2},\frac{\Delta t}{2}\}} ||\mathbf{Y}-\boldsymbol{\Lambda}\boldsymbol{\Xi}\mathbf{U}||_2^2 + Tr\{\boldsymbol{\Xi}\boldsymbol{\Sigma}\boldsymbol{\Xi}^H\}.\end{aligned} \tag{22}$$

The procedure of the proposed adaptive OGSBL method is summarized in Table I. With the estimated $\boldsymbol{\gamma}$, γ_0 and $\boldsymbol{\psi}$, the time-delays of the backscattered echoes can be calculated.

INPUT:

$(2M+2N-2)\times N_s$-dimensional overcomplete dictionary matrix $\boldsymbol{\Xi}$

$(2M+2N-2)\times N_t$-dimensional received signal $\mathbf{Y}$

The number of backscattered echoes K

OUTPUT:

Estimated time-delays $\hat{t}_k$, $k=1,\ 2,\ldots,K$

INITIALIZATION:

Initial parameters γ_k, γ_0 and $\boldsymbol{\psi}$

while not converged ($k<K$) **do**

Calculate $\mathbf{U}$ and $\boldsymbol{\Sigma}$:

$\mathbf{U}=\gamma_0\boldsymbol{\Sigma}(\boldsymbol{\Lambda}\boldsymbol{\Xi})^H\mathbf{Y}$

$\boldsymbol{\Sigma}=\left(\gamma_0(\boldsymbol{\Lambda}\boldsymbol{\Xi})^H\boldsymbol{\Lambda}\boldsymbol{\Xi}+\boldsymbol{\Gamma}^{-1}\right)^{-1}$

UPDATE:

γ_k, γ_0 and $\boldsymbol{\psi}$:

$\gamma_k^{new}=\frac{-N_t+\sqrt{N_t^2+4\rho[\mathbf{U}\mathbf{U}^H+\boldsymbol{\Sigma}]_{k,k}}}{2\rho}$

$\gamma_0^{\text{new}}=\frac{(2M+2N-2)N_t+c-1}{d+||\mathbf{Y}-\boldsymbol{\Lambda}\boldsymbol{\Xi}\mathbf{U}_j||_2^2+N_t tr\left(\boldsymbol{\Lambda}\boldsymbol{\Xi}\boldsymbol{\Sigma}\boldsymbol{\Lambda}\boldsymbol{\Xi}^H\boldsymbol{\Lambda}^H\right)}$

$\boldsymbol{\psi}^{\text{new}}=\arg\min_{\boldsymbol{\psi}\in\{-\frac{\Delta t}{2},\frac{\Delta t}{2}\}}||\mathbf{Y}-\boldsymbol{\Lambda}\boldsymbol{\Xi}\mathbf{U}||_2^2+Tr\{\boldsymbol{\Xi}\boldsymbol{\Sigma}\boldsymbol{\Xi}^H\}$

end while

TABLE I
PROCEDURE OF ADAPTIVE OGSBL METHOD

IV. Simulation Results

In this section, the performance of the proposed co-prime-OGSBL is evaluated with simulated data. The results of MUSIC-MSSP [26], OMP, JOMP and OGSBL are included for comparisons. The number of independent snapshots is 1000, and the signal-to-noise ratio (SNR) is defined as the power ratio of the first backscattered echo to the noise.

A. Simulated Pavement Structures

In both simulations and field experiments, the same UWB step-frequency GPR is used to detect the pavement composed of 3 homogeneous layers, depicted in Fig. 2. Layers 1 and 2 are made up of asphalt, and Layer 3 is a base layer. It can be seen that H_1 and H_2 correspond to the thicknesses of Layers 1 and 2, respectively; ε_{rk}, $k=1,\ 2,\ 3$, denotes the relative permittivity of the kth layer, which are assumed to be known.

$S_0(\tau)$ represents the emitted source signal, while $S_k(\tau_k)$ is the kth backscattered echo from the kth interface with time-delay τ_k and amplitude s_k.

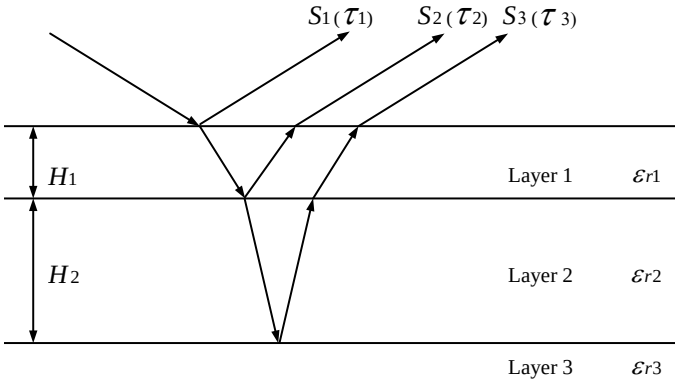

Fig. 2. Pavement configuration.

In the following, two cases are tested with different structures of the pavement and frequency bandwidths from 3 simulations. In Case a, the used frequency bandwidth $B\in[0.5,\ 2.5]$ GHz and 2 backscattered echoes are considered. The pavement structures and sampling strategies are presented in the following sub-cases:

- a_1. $H_1=50$ mm and $H_2=\infty$; $\varepsilon_{r1}=4.5$, $\varepsilon_{r2}=\varepsilon_{r3}=7$; the corresponding times of arrival ($\tau_1,\ \tau_2$) are 1.00 ns and 1.71 ns, respectively. 21 sampling points are applied with $\Delta f=0.1$ GHz for MUSIC-MSSP, OMP, JOMP, and OGSBL; 8 sampling points are used for co-prime-OGSBL with $M=5,\ N=4$. The echoes are non-overlapped.
- a_2. $H_1=20$ mm and $H_2=\infty$; $\varepsilon_{r1}=4.5$, $\varepsilon_{r2}=\varepsilon_{r3}=7$; the corresponding times of arrival ($\tau_1,\ \tau_2$) are 1.00 ns and 1.28 ns, respectively. 21 sampling points are applied with $\Delta f=0.1$ GHz for MUSIC-MSSP, OMP, JOMP, and OGSBL; 8 sampling points are used for co-prime-OGSBL with $M=5,\ N=4$. The echoes are overlapped.
- a_3. $H_1=50$ mm and $H_2=\infty$; $\varepsilon_{r1}=4.5$, $\varepsilon_{r2}=\varepsilon_{r3}=7$; the corresponding times of arrival ($\tau_1,\ \tau_2$) are 1.00 ns and 1.71 ns, respectively. 8 sampling points are applied with $\Delta f=0.25$ GHz for MUSIC-MSSP, OMP, JOMP, OGSBL; 8 sampling points are also used for co-prime-OGSBL with $M=5,\ N=4$. The echoes are non-overlapped.
- a_4. $H_1=20$ mm and $H_2=\infty$; $\varepsilon_{r1}=4.5$, $\varepsilon_{r2}=\varepsilon_{r3}=7$; the corresponding times of arrival ($\tau_1,\ \tau_2$) are 1.00 ns and 1.28 ns, respectively. 8 sampling points are applied with $\Delta f=0.25$ GHz for MUSIC-MSSP, OMP, JOMP, and OGSBL; 8 sampling points are also used for co-prime-OGSBL with $M=5,\ N=4$. The echoes are overlapped.

In Case b, the used frequency bandwidth $B\in[0.5,\ 3.5]$ GHz and 3 backscattered echoes are considered. The pavement structures and sampling strategies are provided in the following sub-cases:

- b_1. $H_1 = 45$ mm and $H_2 = 60$ mm; $\varepsilon_{r1} = 4.5$, $\varepsilon_{r2} = 7$, $\varepsilon_{r3} = 9$; the corresponding times of arrival (τ_1, τ_2, τ_3) are 1.00 ns, 1.64 ns and 2.70 ns, respectively. 31 sampling points are applied with $\Delta f = 0.1$ GHz for MUSIC-MSSP, OMP, JOMP, and OGSBL; 10 sampling points are used for co-prime-OGSBL with $M = 6$, $N = 5$. The echoes are non-overlapped.
- b_2. $H_1 = 15$ mm and $H_2 = 20$ mm; $\varepsilon_{r1} = 4.5$, $\varepsilon_{r2} = 7$, $\varepsilon_{r3} = 9$; the corresponding times of arrival (τ_1, τ_2, τ_3) are 1.00 ns, 1.21 ns and 1.56 ns, respectively. 31 sampling points are applied with $\Delta f = 0.1$ GHz for MUSIC-MSSP, OMP, JOMP, and OGSBL; 10 sampling points are used for co-prime-OGSBL with $M = 6$, $N = 5$. The echoes are overlapped.
- b_3. $H_1 = 45$ mm and $H_2 = 60$ mm; $\varepsilon_{r1} = 4.5$, $\varepsilon_{r2} = 7$, $\varepsilon_{r3} = 9$; the corresponding times of arrival (τ_1, τ_2, τ_3) are 1.00 ns, 1.64 ns and 2.70 ns, respectively. 10 sampling points are applied with $\Delta f = 0.3$ GHz for MUSIC-MSSP, OMP, JOMP, OGSBL; 10 sampling points are also used for co-prime-OGSBL with $M = 6$, $N = 5$. The echoes are non-overlapped.
- b_4. $H_1 = 15$ mm and $H_2 = 20$ mm; $\varepsilon_{r1} = 4.5$, $\varepsilon_{r2} = 7$, $\varepsilon_{r3} = 9$; the corresponding times of arrival (τ_1, τ_2, τ_3) are 1.00 ns, 1.21 ns and 1.56 ns, respectively. 10 sampling points are applied with $\Delta f = 0.3$ GHz for MUSIC-MSSP, OMP, JOMP, OGSBL; 10 sampling points are also used for co-prime-OGSBL with $M = 6$, $N = 5$. The echoes are overlapped.

It should be noted that uniform sampling strategy is necessary to have the following constraint to avoid the spectral ambiguity:

$$\Delta f(\tau_{\max} - \tau_{\min}) \leq 1, \tag{23}$$

where $\tau_{\max}$ and $\tau_{\min}$ are the starting and ending time of the GPR operating period. False peaks may occur with large sampling frequency interval during a given operating period. The co-prime sampling here presents an ambiguity-free manner and has no such limit, which can estimate the time-delays of the backscattered echoes with small number of sampling points [30].

B. Performance from a Single Run of Algorithms

In the first simulation, the co-prime-OGSBL with the extended radar data model and the compared methods are tested in a single run of the algorithms. Both Cases a and b are studied.

Figs. 3-4 show pseudo-spectra of the co-prime-OGSBL and the compared methods (MUSIC-MSSP, OMP, JOMP, and OGSBL) with different pavements, frequency bandwidths and sample points. In Fig. 3, a pavement of two layers is studied with different thicknesses. In Figs. 3(a) and 3(c), the thickness of layers is 50 mm, and two backscattered echoes are non-overlapped with product $B\Delta\tau \geq 1$. Two peaks correspond to the true time-delays, which are well estimated by all the methods in Fig. 3(a). In Fig. 3(c), due to large sampling frequency difference $\Delta f(\tau_{\max} - \tau_{\min}) \geq 1$, ambiguity occurs in MUSIC-MSSP and OGSBL with repeated copies of false peaks, while OMP and JOMP fails in TDE. Nevertheless,

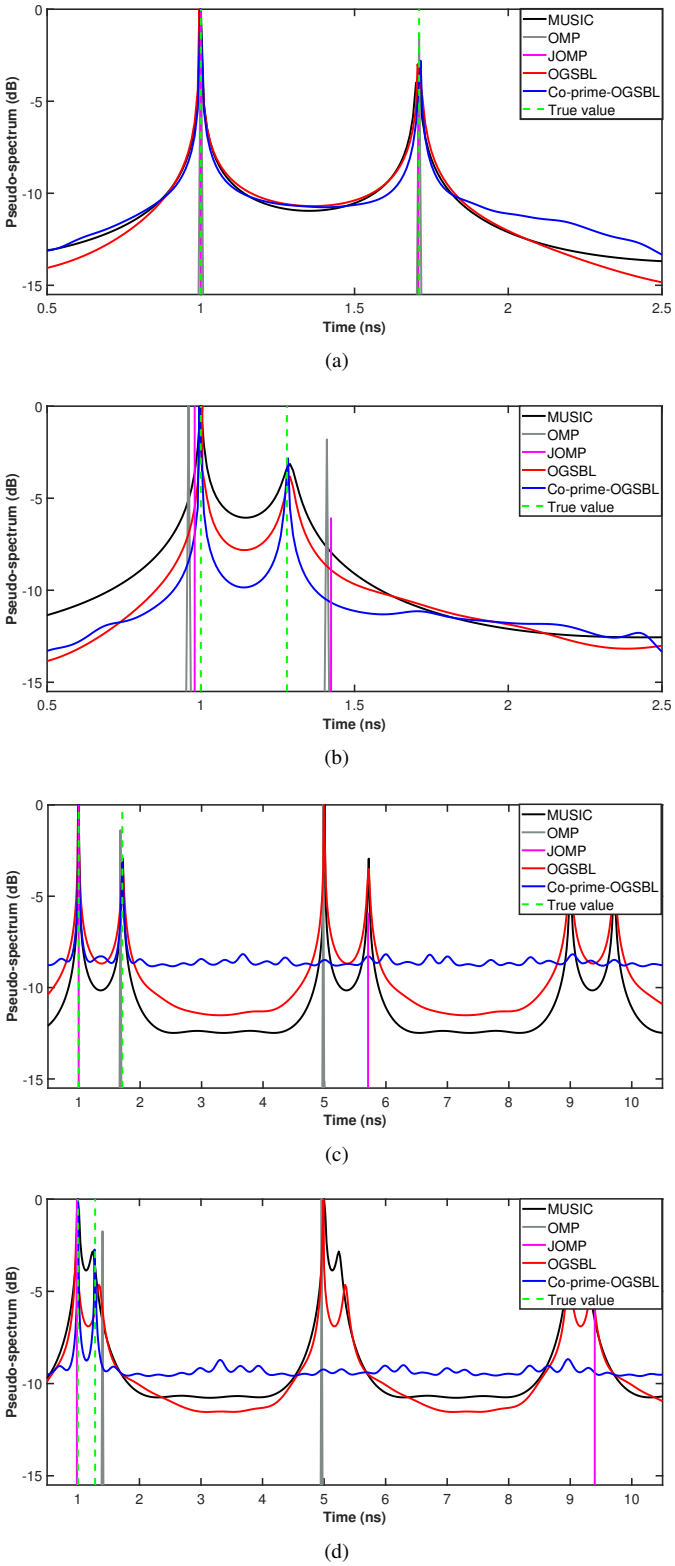

Fig. 3. Case a with 1000 snapshots and SNR = 10 dB, Pseudo-spectra of MUSIC-MSSP, OMP, JOMP OGSBL, and co-prime-OGSBL for TDE of 2 backscattered echoes. (a) $\tau_1 = 1.00$ ns, $\tau_2 = 1.71$ ns; 21 sampling points are used for MUSIC-MSSP, OMP, JOMP, and OGSBL, 8 sampling points are used for co-prime-OGSBL; (b) $\tau_1 = 1.00$ ns, $\tau_2 = 1.28$ ns; 21 sampling points are used for MUSIC-MSSP, OMP, JOMP, and OGSBL, 8 sampling points are used for co-prime-OGSBL; (c) $\tau_1 = 1.00$ ns, $\tau_2 = 1.71$ ns; 8 sampling points are used for MUSIC-MSSP, OMP, JOMP, OGSBL, and co-prime-OGSBL; (d) $\tau_1 = 1.00$ ns, $\tau_2 = 1.28$ ns; 8 sampling points are used for MUSIC-MSSP, OMP, OMP, JOMP, OGSBL, and co-prime-OGSBL.

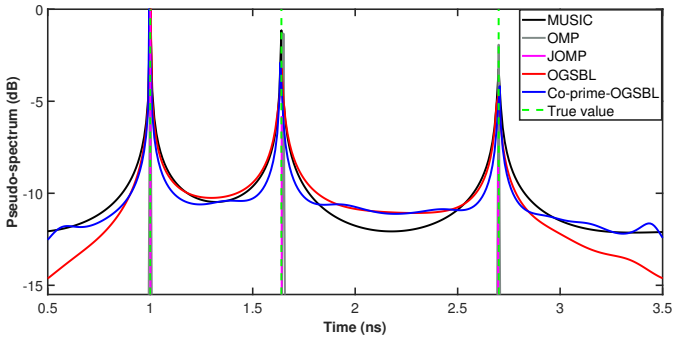

(a)

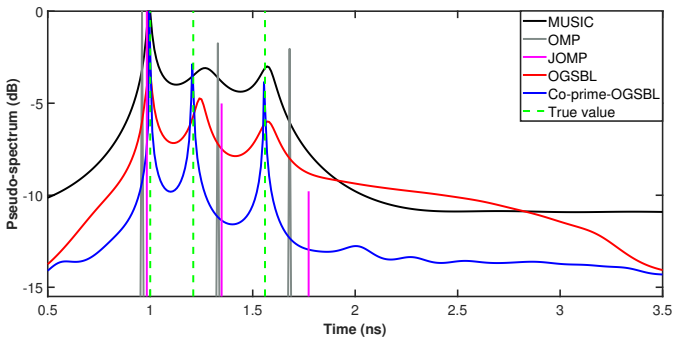

(b)

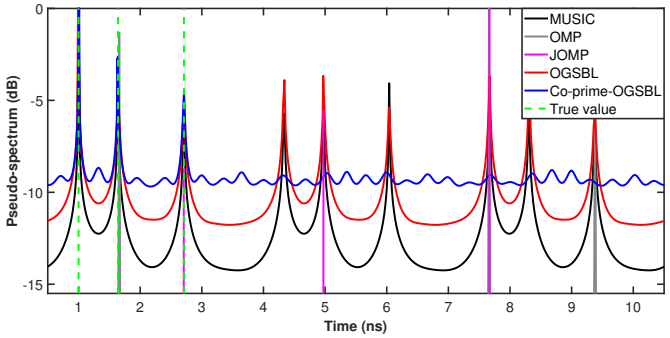

(c)

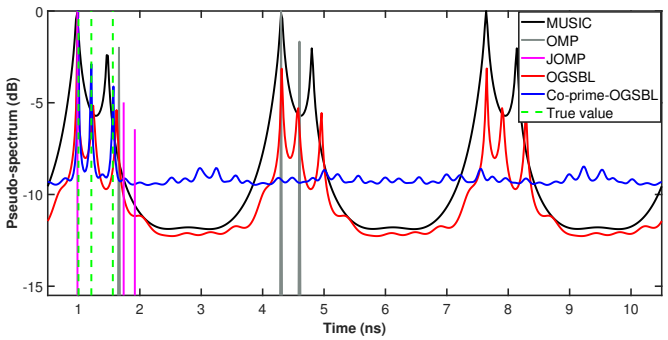

(d)

Fig. 4. Case b with 1000 snapshots and SNR = 10 dB, Pseudo-spectra of MUSIC-MSSP, OMP, JOMP OGSBL, and co-prime-OGSBL for TDE of 3 backscattered echoes. (a) $\tau_1 = 1.00$ ns, $\tau_2 = 1.64$ ns and $\tau_3 = 2.70$ ns; 31 sampling points are used for MUSIC-MSSP, OMP, JOMP, and OGSBL, 10 sampling points are used for co-prime-OGSBL; (b) $\tau_1 = 1.00$ ns, $\tau_2 = 1.21$ ns and $\tau_3 = 1.56$ ns; 31 sampling points are used for MUSIC-MSSP, OMP, JOMP, and OGSBL, 10 sampling points are used for co-prime-OGSBL; (c) $\tau_1 = 1.00$ ns, $\tau_2 = 1.64$ ns and $\tau_3 = 2.70$ ns; 10 sampling points are used for MUSIC-MSSP, OMP, JOMP, OGSBL, and co-prime-OGSBL; (d) $\tau_1 = 1.00$ ns, $\tau_2 = 1.21$ ns and $\tau_3 = 1.56$ ns; 10 sampling points are used for MUSIC-MSSP, OMP, JOMP, OGSBL, and co-prime-OGSBL.

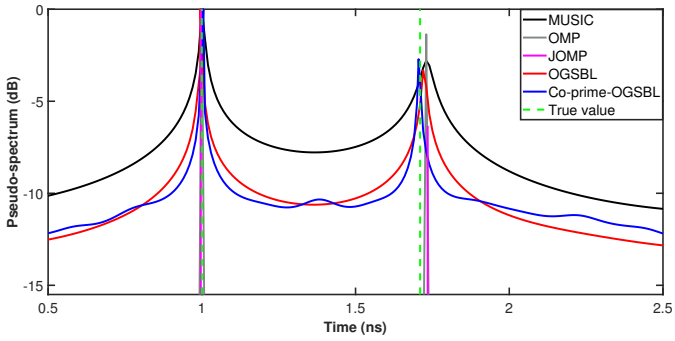

(a)

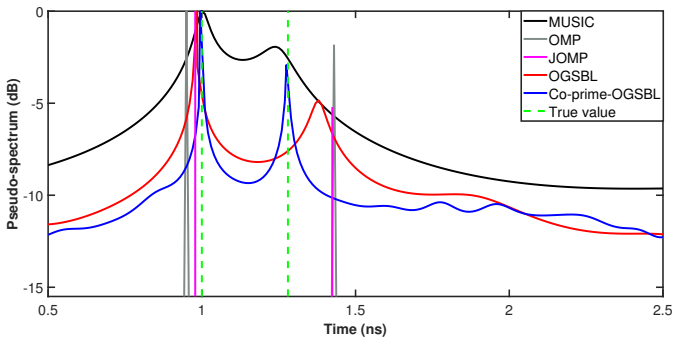

(b)

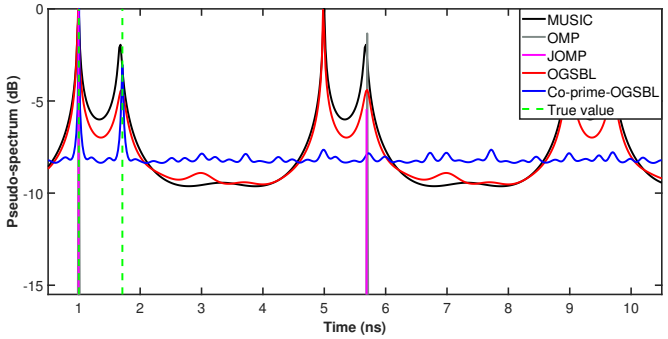

(c)

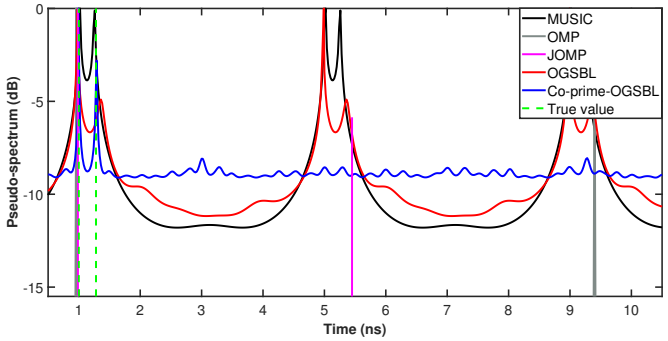

(d)

Fig. 5. Case a with single snapshot and SNR = 30 dB, Pseudo-spectra of MUSIC-MSSP, OMP, JOMP OGSBL, and co-prime-OGSBL for TDE of 2 backscattered echoe. (a) $\tau_1 = 1.00$ ns, $\tau_2 = 1.71$ ns; 21 sampling points are used for MUSIC-MSSP, OMP, JOMP, and OGSBL, 8 sampling points are used for co-prime-OGSBL; (b) $\tau_1 = 1.00$ ns, $\tau_2 = 1.28$ ns; 21 sampling points are used for MUSIC-MSSP, OMP, JOMP, and OGSBL, 8 sampling points are used for co-prime-OGSBL; (c) $\tau_1 = 1.00$ ns, $\tau_2 = 1.71$ ns; 8 sampling points are used for MUSIC-MSSP, OMP, JOMP, OGSBL, and co-prime-OGSBL; (d) $\tau_1 = 1.00$ ns, $\tau_2 = 1.28$ ns; 8 sampling points are used for MUSIC-MSSP, OMP, JOMP, OGSBL, and co-prime-OGSBL.

TABLE II
ESTIMATED TIME-DELAYS IN CASE a

Method	case a_1		case a_2		case a_3		case a_4	
	t_1	t_2	t_1	t_2	t_1	t_2	t_1	t_2
True value	1.000	1.710	1.000	1.270	1.000	1.710	1.000	1.270
MUSIC	1.000	1.710	1.000	1.270	/	/	/	/
OMP	1.000	1.710	0.960	1.410	1.680	4.980	1.741	4.960
JOMP	1.000	1.710	0.979	1.427	1.023	5.709	0.983	9.398
OGSBL	0.995	1.705	0.989	1.340	/	/	/	/
Co-prime-OGSBL	0.998	1.712	0.995	1.279	1.008	1.710	0.996	1.287

"/" denotes that there is no available solution. The time-delay estimation results are in nanosecond (ns).

by exploiting the co-prime sampling strategy, the co-prime-OGSBL can accurately estimate the time-delays without ambiguity. Similar performance can be found in Figs. 4(a) and 4(c) with 3 layers ($H_1 = 45$ mm and $H_2 = 60$ mm, 3 backscattered echoes are non-overlapped).

In Figs. 3(b) and 3(d), the thickness of layers is 20 mm, where two backscattered echoes are overlapped with product $B\Delta\tau \leq 1$. In Fig. 3(b), OMP and JOMP fails in TDE; OGSBL estimates time-delays of backscattered echoes with bias because of limited resolution power, while MUSIC-MSSP and the proposed co-prime-OGSBL perform well in TDE. However, in Fig. 3(d), MUSIC-MSSP, OMP, JOMP and OGSBL cannot estimate the time-delays because of large sampling frequency difference, while the co-prime-OGSBL is still robust in TDE. In Figs. 4(b) and 4(d), a pavement with 3 layers is studied with $H_1 = 15$ mm and $H_2 = 20$ mm, and 3 backscattered echoes are overlapped. The estimation performance is similar to that of Figs. 3(b) and 3(d), and the co-prime-OGSBL performs best in Figs. 4(b) and 4(d), while MUSIC-MSSP cannot detect true time-delays of the backscattered echoes owing to its resolution capability in Fig. 4(b). TABLEs II and III display the results of algorithms in the above simulations, among which the proposed co-prime-OGSBL performs stably with higher accuracy compared with the four competitors.

In Fig. 5, we evaluate the performance of the proposed co-prime-OGSBL and the competitors under finite snapshots. The pavement structures and sampling strategies are the same as those in case a except for single snapshot and SNR = 30 dB. Figs. 5(a) and 5(c) show the performance pseudo-spectra of algorithms when $B\Delta\tau \geq 1$ while Figs. 5(b) and 5(d) give the results of two overlapped echoes with $B\Delta\tau = 0.56$. According to Figs 5, some methods fail in the estimation of time-delay due to limited temporal resolution, for example, OMP and JOMP; some methods show false peaks with repeated periods, such as MUSIC-SSP and OGSBL using 8-point uniform sampling in Figs. 5(c) and 5(d). The proposed co-prime-OGSBL yields effective, unambiguous, and accurate estimation performance even with single snapshot.

C. Statistical Performance versus SNR

In the second simulation, the statistical performance of co-prime-OGSBL and its competitors is evaluated with 200 independent runs. The relative root mean square error (RRMSE) on the estimated thickness as a function of SNR is calculated. A pavement of two layers is considered (two backscattered echoes), SNR $\in [0, 20]$ dB. The simulation parameters are the same with Cases a_1 and a_2. The GPR operating period is $t \in [0.5, 2.5]$ ns.

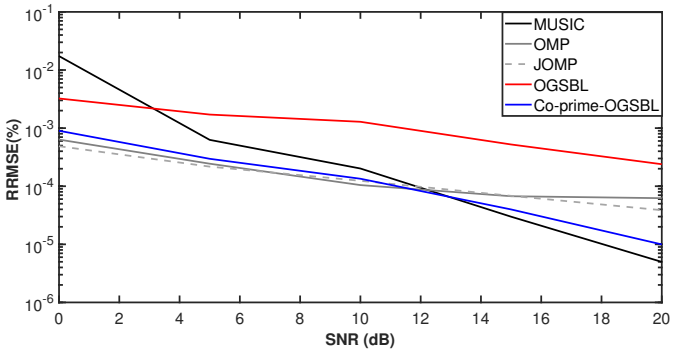

Fig. 6. RRMSE on the estimated thickness $\hat{H}_1$ versus SNR, non-overlapped echoes (Case a_1). $B\Delta\tau = 1.42$.

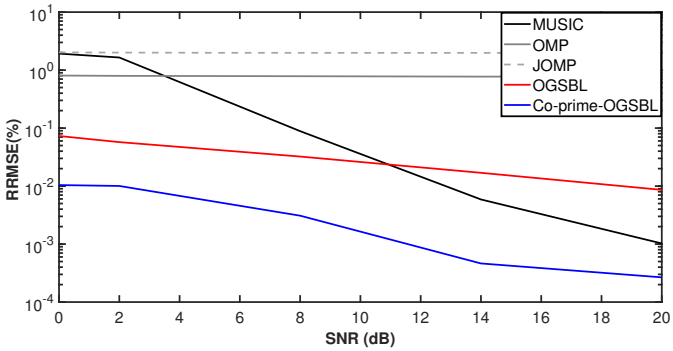

Fig. 7. RRMSE on the estimated thickness $\hat{H}_1$ versus SNR, overlapped echoes (Case a_2). $B\Delta\tau = 0.56$.

Figs. 6-7 present the RRMSEs on the estimated thickness by the co-prime-OGSBL and its competitors as function of SNR. The RRMSEs of the co-prime-OGSBL, OGSBL and MUSIC-MSSP continuously decrease with the increase of SNR for both Cases a_1 and a_2 (overlapped and non-overlapped echoes), while OMP and JOMP show their biased performance in the scenario of overlapped echoes. When it comes to non-overlapped echoes, the estimation performance of above

TABLE III
ESTIMATED TIME-DELAYS IN CASE b

Method	case b_1			case b_2			case b_3			case b_4		
	t_1	t_2	t_3	t_1	t_2	t_3	t_1	t_2	t_3	t_1	t_2	t_3
True value	1.000	1.640	2.700	1.000	1.210	1.560	1.000	1.640	2.700	1.000	1.210	1.560
MUSIC	1.000	1.640	2.700	0.990	1.270	1.570	/	/	/	/	/	/
OMP	1.000	1.650	2.700	0.960	1.330	1.680	1.660	7.667	9.380	1.660	4.300	4.600
JOMP	1.004	1.653	2.474	0.989	1.348	1.773	2.710	4.970	7.667	0.984	1.736	1.918
OGSBL	0.995	1.635	2.695	0.995	1.241	1.570	/	/	/	/	/	/
Co-prime-OGSBL	1.002	1.635	2.705	0.998	1.209	1.561	0.998	1.645	2.700	0.997	1.208	1.562

"/" denotes that there is no available solution. The time-delay estimation results are in nanosecond (ns).

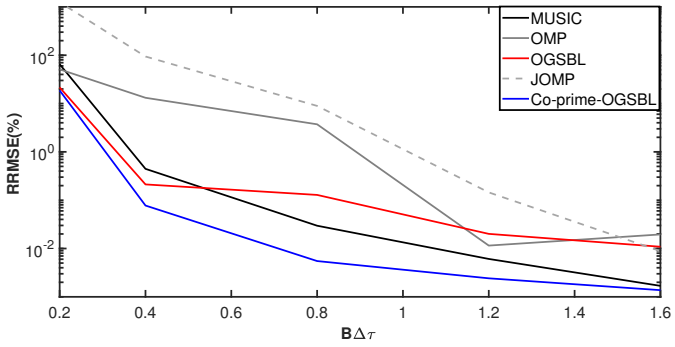

Fig. 8. RRMSE on the estimated time-delay $\widehat{\Delta\tau}$ as function of $B\Delta\tau$ product at SNR= 10 dB.

mentioned methods tends to be similar. Overall, the co-prime-OGSBL has better estimation performance than OMP, JOMP MUSIC, and OGSBL, especially in the scenario of overlapped echoes and high-SNR level.

D. Statistical Performance versus $B\Delta\tau$ Product

In the last simulation, the resolution power of the proposed co-prime-OGSBL is evaluated as a function of the $B\Delta\tau$ products. Consider a pavement of two layers, the layer thickness $H \in [7.1,\ 53.0]$ mm, the corresponding $B\Delta\tau$ product changes from 0.2 to 1.5. SNR is fixed at 10 dB. Other simulation parameters are the same with those of Case a_1. The RRMSEs of the co-prime-OGSBL and its competitors as a function of the product $B\Delta\tau$ are evaluated by a Monte-Carlo process of 200 independent runs. The radar pulse can be measured as the echo backscattered from a metallic plane.

Fig. 8 shows the RRMSEs of the estimated time-delay ($\widehat{\Delta\tau}$). In the beginning, $B\Delta\tau = 0.2$, all the methods fail in TDE. Then, with the increase of $B\Delta\tau$ product, the RRMSEs of $\widehat{\Delta\tau}$ continuously decrease. The proposed method has enhanced resolution power (with smaller RRMSE), which outperforms MUSIC, OMP, JOMP and OGSBL.

In addition, the runtime for a single run of the proposed method and OGSBL (Case a_1) is measured. By using the co-prime sampling strategy, the computational complexity of the proposed method (0.229 s) is much lower than that of the OGSBL (0.451 s) with a computer equipped with a CPU of 3.0 GHz and 32 GB of RAM.

V. EXPERIMENTAL RESULTS

In this section, the experimental results of the proposed co-prime-OGSBL, MUSIC-MSSP, OMP, JOMP and OGSBL are presented. An UWB step-frequency GPR based on a vector network analyzer (VNA) and two zero-offset antennas (ETSA A5 antennas) has been applied for pavement survey during a long term experiment at the fatigue carousel [52], [53]. As shown in Fig. 9, a pair of air-launched horn antennas, called the transmitter (Tx) and receiver (Rx), are close to each other and fixed at 70.0 cm above the tested pavement, which satisfies the far-field condition. The automatic working platform allows moving the Tx-Rx antennas in the direction of pavement detection as shown in Fig. 10. The frequency bandwidth of the step-frequency GPR signal is $B \in [0.8,\ 10.8]$ GHz. By using the uniform sampling strategy, the number of sample points is 401 with a frequency step of 0.025 GHz.

According to [54], the studied asphalt pavement is made of three interfaces separating media, as depicted in Fig. 9. The layers $\Omega_1(\epsilon_{r1})$, $\Omega_2(\epsilon_{r2})$ and $\Omega_3(\epsilon_{r3})$ are the asphalt layer, sand layer and base-layer, respectively. Layer $\Omega_2(\epsilon_{r2})$ is very thin with thickness (H_2) less than 1 cm, which represents some artificial debonding defect embedded within the pavement structure. Based on [53], the sand is proven to be wet by using destructive testing method, therefore, the permittivity of this layer is about 25 [44]. The length of the studied asphalt pavement is about 30 cm with a sample step 1 cm (30 sample points). For each sample point, a single snapshot is implemented.

A. Data Set

The GPR is moved slightly between different sample points in order to obtain independent measurements in time domain. Fig. 11 presents the backscattered echoes from the studied pavement by raw experimental data (B-scan). Time filtering, a preprocessing technique, is applied to eliminate the echoes like multiple echoes and air wave outside the GPR working time window or the region of interest [17].

It can be seen from Fig. 11 that two peaks corresponding to the first three echoes backscattered from the first three interfaces: the first peak represents the echo backscattered from

Fig. 9. Experimental configuration.

Fig. 10. GPR Data collection at the fatigue carousel using a pair of robot-controlled bistatic antennas over the pavement test area.

the top surface (first echo); the second peak corresponds to the second and third backscattered echoes from the debonding layer with a very small embedded sand thickness. The first backscattered echo is clearly visible in Fig. 11. The echoes from the second and third interfaces of the sand layer are overlapped and cannot be distinguished from GPR data. In the following, we focus on the estimation of the second and third backscattered echoes, the small thickness of sand layer. The first echo will be removed by time filtering after it is detected by the proposed method.

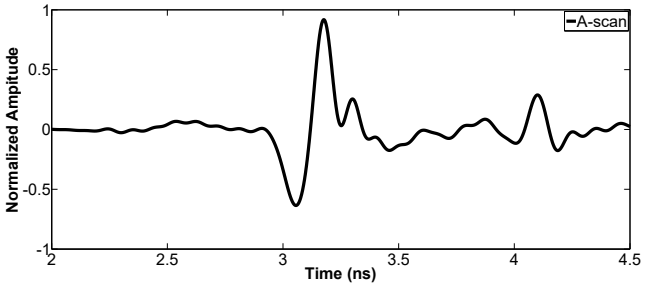

(a)

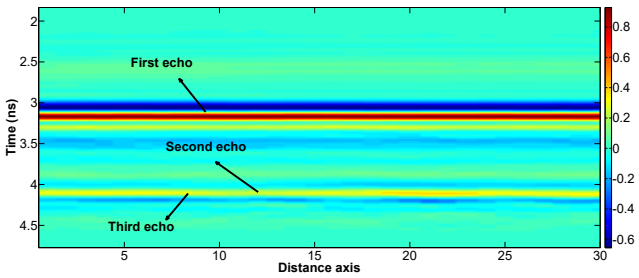

(b)

Fig. 11. GPR data collected at the pavement fatigue carousel test-site. (a) A-scan of raw data; (b) B-scan.

B. Time-Delay and Thickness Estimation

In the experiment, the co-prime-OGSBL is tested within frequency bandwidth $B = [0.8, 4.8]$ GHz at the 15th sample point of the studied asphalt pavement.

By using the co-prime sampling strategy with co-prime integers $M = 7$ and $N = 6$, 12 frequency sample points are used for co-prime-OGSBL. While for OMP, JOMP OGSBL and MUSIC-MSSP, uniform sampling strategy is applied with 161 samples. Then, the co-prime-OGSBL is applied to estimate the time-delays ($\widehat{\Delta\tau}$) of the second and third backscattered echoes. Finally, the thickness of the sand layer can be calculated from following equation:

$$\widehat{H}_2 = \frac{c\widehat{\Delta\tau}}{2\sqrt{\varepsilon_{r3}}} \tag{24}$$

where $\widehat{H}_2$ is the estimated thickness of the sand layer; c the speed of light in vacuum, and ε_{r3} the permittivity of wet sand layer. Table IV shows the estimated time-delay $\widehat{\Delta\tau}$ and thickness $\widehat{H}_2$ of the sand layer. Compared with that of MUSIC, OMP and OGSBL, the estimated thickness by the co-prime-OGSBL is close to the true value ($H_2 \approx 0.3 \sim 0.4$ cm), which means that the proposed method has high estimation accuracy in real GPR detection. True value of H_2 is obtained by drilling a vertical hole at a tested point.

TABLE IV
ESTIMATED TIME-DELAY AND THICKNESS

Method \ Parameter	$\widehat{\Delta\tau}$	$\widehat{H}_2$
MUSIC	0.221 ns	0.66 cm
OMP	0.200 ns	0.60 cm
OGSBL	0.150 ns	0.45 cm
Co-prime-OGSBL	0.121 ns	0.36 cm

VI. CONCLUSION

In this paper, we propose a co-prime sampling strategy based OGSBL, namely co-prime-OGSBL, to estimate time-delay and thickness of roadway for intelligent transportation systems. Different from the uniform sampling strategy of GPR, the co-prime-OGSBL exploits the merits of co-prime sparse sampling, which uses much fewer frequency sampling points (low complexity) but reaches similar, or even better estimation performance than the conventional GPR methods. The OGSBL is adapted to GPR data processing by taking into account the radar pulse, non-circularity of GPR signals and co-prime sampling, which can achieve high resolution and accuracy in TDE of thin layers. Both numerical and experimental results demonstrate the effectiveness of the proposed method. In the future, we will work on the thickness estimation without the *a priori* knowledge of permittivity of media and other sparse sampling strategies.

REFERENCES

[1] Y. Shi, L. Cui, Z. Qi, F. Meng, and Z. Chen, "Automatic road crack detection using random structured forests," *IEEE Transactions on Intelligent Transportation Systems*, vol. 17, no. 12, pp. 3434–3445, 2016.

[2] W. W. Lai, R. K. Chang, and J. F. Sham, "A blind test of nondestructive underground void detection by ground penetrating radar (GPR)," *Journal of Applied Geophysics*, vol. 149, pp. 10–17, 2018.

[3] C. Le Bastard, J. Pan, Y. Wang, M. Sun, S. S. Todkar, V. Baltazart, N. Pinel, A. Ihamouten, X. Dérobert, and C. Bourlier, "A linear prediction and support vector regression-based debonding detection method using step-frequency ground penetrating radar," *IEEE Geoscience and Remote Sensing Letters*, vol. 16, no. 3, pp. 367–371, 2018.

[4] L. Zou, L. Yi, and M. Sato, "On the use of lateral wave for the interlayer debonding detecting in an asphalt airport pavement using a multistatic GPR system," *IEEE Transactions on Geoscience and Remote Sensing*, vol. 58, no. 6, pp. 4215–4224, 2020.

[5] N. S. P. Peraka and K. P. Biligiri, "Pavement asset management systems and technologies: A review," *Automation in Construction*, vol. 119, p. 103336, 2020.

[6] C. Han, T. Ma, L. Gu, J. Cao, X. Shi, W. Huang, and Z. Tong, "Asphalt pavement health prediction based on improved transformer network," *IEEE Transactions on Intelligent Transportation Systems*, pp. 1–12, 2022.

[7] S. Mathavan, K. Kamal, and M. Rahman, "A review of three-dimensional imaging technologies for pavement distress detection and measurements," *IEEE Transactions on Intelligent Transportation Systems*, vol. 16, no. 5, pp. 2353–2362, 2015.

[8] Y. Hou, Q. Li, C. Zhang, G. Lu, Z. Ye, Y. Chen, L. Wang, and D. Cao, "The state-of-the-art review on applications of intrusive sensing, image processing techniques, and machine learning methods in pavement monitoring and analysis," *Engineering*, vol. 7, no. 6, pp. 845–856, 2021.

[9] Z. Du, J. Yuan, F. Xiao, and C. Hettiarachchi, "Application of image technology on pavement distress detection: A review," *Measurement*, vol. 184, p. 109900, 2021.

[10] S. Wang, X. Sui, Z. Leng, J. Jiang, and G. Lu, "Asphalt pavement density measurement using non-destructive testing methods: current practices, challenges, and future vision," *Construction and Building Materials*, vol. 344, p. 128154, 2022.

[11] W. Lai, X. Dérobert, and P. Annan, "A review of ground penetrating radar application in civil engineering: A 30-year journey from locating and testing to imaging and diagnosis," *NDT & E International*, vol. 96, pp. 58–78, 2018.

[12] N. Kim, S. Kim, Y. An, and J. Lee, "Triplanar imaging of 3D GPR data for deep-learning-based underground object detection," *IEEE Journal of Selected Topics in Applied Earth Observations and Remote Sensing*, vol. 12, no. 11, pp. 4446–4456, 2019.

[13] F. Giovanneschi, K. V. Mishra, M. A. Gonzalez-Huici, Y. C. Eldar, and J. H. Ender, "Dictionary learning for adaptive GPR landmine classification," *IEEE Transactions on Geoscience and Remote Sensing*, vol. 57, no. 12, pp. 10036–10055, 2019.

[14] F. D'Amico, V. Gagliardi, L. B. Ciampoli, and F. Tosti, "Integration of InSAR and GPR techniques for monitoring transition areas in railway bridges," *NDT & E International*, vol. 115, p. 102291, 2020.

[15] N. Rees, K. Thiyagarajan, S. Wickramanayake, and S. Kodagoda, "Ground-penetrating radar signal characterization for non-destructive evaluation of low-range concrete sub-surface boundary conditions," *IEEE Sensors Letters*, vol. 6, no. 4, pp. 1–4, 2022.

[16] C. Le Bastard, V. Baltazart, Y. Wang, and J. Saillard, "Thin-pavement thickness estimation using GPR with high-resolution and superresolution methods," *IEEE Transactions on Geoscience and Remote Sensing*, vol. 45, no. 8, pp. 2511–2519, 2007.

[17] J. Pan, M. Sun, Y. Wang, C. Le Bastard, and V. Baltazart, "Time delay estimation by a modified orthogonal matching pursuit method for rough pavement," *IEEE Transactions on Geoscience and Remote Sensing*, vol. 59, no. 4, pp. 2973–2981, 2021.

[18] I. Al-Qadi and S. Lahouar, "Measuring layer thicknesses with GPR–theory to practice," *Construction and building materials*, vol. 19, no. 10, pp. 763–772, 2005.

[19] S. Zhao and I. L. Al-Qadi, "Super-resolution of 3-D GPR signals to estimate thin asphalt overlay thickness using the XCMP method," *IEEE Transactions on Geoscience and Remote sensing*, vol. 57, no. 2, pp. 893–901, 2018.

[20] M. Sun, C. Le Bastard, Y. Wang, N. Pinel, J. Pan, V. Baltazart, J.-M. Simonin, and X. Dérobert, "Time delay and interface roughness estimation using modified ESPRIT with interpolated spatial smoothing technique," *IEEE Transactions on Geoscience and Remote Sensing*, vol. 56, no. 3, pp. 1475–1484, 2018.

[21] S. Zhao and I. L. Al-Qadi, "Super-resolution of 3-D GPR signals to estimate thin asphalt overlay thickness using the XCMP method," *IEEE Transactions on Geoscience and Remote Sensing*, vol. 57, no. 2, pp. 893–901, 2019.

[22] J. Pan, M. Sun, Y. Wang, C. Le Bastard, and V. Baltazart, "A time-delay estimation approach for coherent GPR signals by taking into account the noise pattern and radar pulse," *Signal Processing*, vol. 176, p. 107654, 2020.

[23] B. Tchana Tankeu, V. Baltazart, Y. Wang, and D. Guilbert, "PUMA applied to time delay estimation for processing GPR data over debonded pavement structures," *Remote Sensing*, vol. 13, no. 17, p. 3456, 2021.

[24] J. Pan, M. Sun, Y. Wang, and X. Zhang, "An Enhanced Spatial Smoothing Technique With ESPRIT Algorithm for Direction of Arrival Estimation in Coherent Scenarios," *IEEE Transactions on Signal Processing*, vol. 68, pp. 3635–3643, 2020.

[25] A. Benedetto, F. Tosti, L. B. Ciampoli, and F. D'amico, "An overview of ground-penetrating radar signal processing techniques for road inspections," *Signal processing*, vol. 132, pp. 201–209, 2017.

[26] M. Sun, J. Pan, C. Le Bastard, Y. Wang, and J. Li, "Advanced signal processing methods for ground-penetrating radar: Applications to civil engineering," *IEEE Signal Processing Magazine*, vol. 36, no. 4, pp. 74–84, 2019.

[27] Z. Tong, J. Gao, and D. Yuan, "Advances of deep learning applications in ground-penetrating radar: A survey," *Construction and Building Materials*, vol. 258, p. 120371, 2020.

[28] C. Zhou, Z. Shi, Y. Gu, and X. Shen, "DECOM: DOA estimation with combined MUSIC for coprime array," in *2013 International Conference on Wireless Communications and Signal Processing*, pp. 1–5, 2013.

[29] P. Pal and P. P. Vaidyanathan, "Coprime sampling and the MUSIC algorithm," in *2011 Digital Signal Processing and Signal Processing Education Meeting (DSP/SPE)*, pp. 289–294, 2011.

[30] Z. Fu, P. Chargé, and Y. Wang, "Multi-rate coprime sampling for frequency estimation with increased degrees of freedom," *Signal Processing*, vol. 166, p. 107258, 2020.

[31] P. Pal and P. P. Vaidyanathan, "Nested arrays: A novel approach to array processing with enhanced degrees of freedom," *IEEE Transactions on Signal Processing*, vol. 58, no. 8, pp. 4167–4181, 2010.

[32] Z. Zheng, Y. Huang, W.-Q. Wang, and H. C. So, "Direction-of-Arrival Estimation of Coherent Signals via Coprime Array Interpolation," *IEEE Signal Processing Letters*, vol. 27, pp. 585–589, 2020.

[33] X. Zhang, Z. Zheng, W.-Q. Wang, and H. C. So, "DOA Estimation of Coherent Sources Using Coprime Array via Atomic Norm Minimization," *IEEE Signal Processing Letters*, vol. 29, pp. 1312–1316, 2022.

[34] J. Li, C. Le Bastard, Y. Wang, G. Wei, B. Ma, and M. Sun, "Enhanced GPR signal for layered media time-delay estimation in low-SNR scenario," *IEEE Geoscience and Remote Sensing Letters*, vol. 13, no. 3, pp. 299–303, 2016.

[35] M. Sun, J. Pan, Y. Wang, X. Zhang, X. Xiao, C. Fauchard, and C. L. Bastard, "Time-delay estimation by enhanced orthogonal matching pursuit method for thin asphalt pavement with similar permittivity," *IEEE Transactions on Intelligent Transportation Systems*, vol. 23, no. 7, pp. 8940–8948, 2022.

[36] J. Tropp, A. Gilbert, and M. Strauss, "Simultaneous sparse approximation via greedy pursuit," in *Proceedings. (ICASSP '05). IEEE International Conference on Acoustics, Speech, and Signal Processing, 2005.*, vol. 5, pp. v/721–v/724 Vol. 5, 2005.

[37] Z. Tan and A. Nehorai, "Sparse direction of arrival estimation using co-prime arrays with off-grid targets," *IEEE Signal Processing Letters*, vol. 21, no. 1, pp. 26–29, 2014.

[38] S. Yang, B. Liu, Z. Hong, and Z. Zhang, "Low-complexity sparse array synthesis based on off-grid compressive sensing," *IEEE Antennas and Wireless Propagation Letters*, vol. 21, no. 12, pp. 2322–2326, 2022.

[39] Z. Yang, L. Xie, and C. Zhang, "Off-grid direction of arrival estimation using sparse Bayesian inference," *IEEE transactions on signal processing*, vol. 61, no. 1, pp. 38–43, 2013.

[40] J. A. Tropp and A. C. Gilbert, "Signal recovery from random measurements via orthogonal matching pursuit," *IEEE Transactions on information theory*, vol. 53, no. 12, pp. 4655–4666, 2007.

[41] Z. Yang, L. Xie, and C. Zhang, "Off-Grid Direction of Arrival Estimation Using Sparse Bayesian Inference," *IEEE Transactions on Signal Processing*, vol. 61, no. 1, pp. 38–43, 2013.

[42] Z. Yang, J. Li, P. Stoica, and L. Xie, "Chapter 11 - sparse methods for direction-of-arrival estimation," in *Academic Press Library in Signal Processing, Volume 7* (R. Chellappa and S. Theodoridis, eds.), pp. 509–581, Academic Press, 2018.

[43] C. Fauchard, *Utilisation de radars très hautes fréquences: application à l'auscultation non destructive des chaussées*. PhD thesis, 2001.

[44] D. J. Daniels, *Ground penetrating radar*, vol. 1st edition. IET, 2004.

[45] P. Chargé, Y. Wang, and J. Saillard, "A non-circular sources direction finding method using polynomial rooting," *Signal Processing*, vol. 81, no. 8, pp. 1765–1770, 2001.

[46] X. Zhang, X. Lai, W. Zheng, and Y. Wang, "Sparse Array Design for DOA Estimation of Non-Circular Signals: Reduced Co-Array Redundancy and Increased DOF," *IEEE Sensors Journal*, vol. 21, no. 24, pp. 27928–27937, 2021.

[47] H. Abeida and J.-P. Delmas, "MUSIC-like estimation of direction of arrival for noncircular sources," *IEEE Transactions on Signal Processing*, vol. 54, no. 7, pp. 2678–2690, 2006.

[48] F. Yang, L. Zhang, S. Yu, D. Prokhorov, X. Mei, and H. Ling, "Feature pyramid and hierarchical boosting network for pavement crack detection," *IEEE Transactions on Intelligent Transportation Systems*, vol. 21, no. 4, pp. 1525–1535, 2020.

[49] S. Ji, Y. Xue, and L. Carin, "Bayesian compressive sensing," *IEEE Transactions on signal processing*, vol. 56, no. 6, pp. 2346–2356, 2008.

[50] M. Carlin, P. Rocca, G. Oliveri, F. Viani, and A. Massa, "Directions-of-arrival estimation through Bayesian compressive sensing strategies," *IEEE Transactions on Antennas and Propagation*, vol. 61, no. 7, pp. 3828–3838, 2013.

[51] M. E. Tipping, "Sparse Bayesian learning and the relevance vector machine," *Journal of Machine Learning Research*, vol. 1, no. Jun, pp. 211–244, 2001.

[52] P. Hornych, J.-P. Kerzrého, J. Sohm, A. Chabot, S. Trichet, J.-L. Joutang, and N. Bastard, "Full scale tests on grid reinforced flexible pavements on the french fatigue carrousel," in *7th RILEM International Conference on Cracking in Pavements*, pp. 1251–1260, Springer, 2012.

[53] X. Dérobert, V. Baltazart, J.-M. Simonin, S. S. Todkar, C. Norgeot, and H.-Y. Hui, "GPR monitoring of artificial debonded pavement structures throughout its life cycle during accelerated pavement testing," *Remote Sensing*, vol. 13, no. 8, p. 1474, 2021.

[54] J.-M. Simonin, V. Baltazart, C. L. Bastard, and X. Derobert, "Progress in monitoring the debonding within pavement structures during accelerated pavement testing on the fatigue carousel," in *8th RILEM International Conference on Mechanisms of Cracking and Debonding in Pavements*, pp. 749–755, Springer, 2016.